Nano Research

Open Access

Research Article

High-performance press-driven triboelectric nanogenerator based on a gear acceleration structure and its application in ultraviolet sensors

Taimin Ren[1,2], Cong Zhai[2] ✉, Zekun Wang[1], Congcong Hao[1], Mingzhe Cai[1], Yongqiu Zheng[1], and Chenyang Xue[1,2]

[1] *Key Laboratory of Instrumentation Science & Dynamic Measurement Ministry of Education, North University of China, Taiyuan 030051, China*
[2] *Laoshan Laboratory, Qingdao 266237, China*

Cite this article: *Nano Research*, **2025**, *18*, 94907401. https://doi.org/10.26599/NR.2025.94907401

ABSTRACT: Triboelectric nanogenerator (TENG) is an innovative energy technology that converts mechanical energy into electrical energy by utilizing the triboelectric effect and the principle of static electric induction. Rotary triboelectric nanogenerator (R-TENG) can collect mechanical energy from the surrounding environment, but its shortcomings such as too large collection device and insufficient wear resistance hinder its further development. In this study, we propose a high-performance press-driven rotation triboelectric nanogenerator (HPR-TENG), which uses a gear acceleration structure to achieve efficient energy conversion by pressing, and significantly improves the output performance and durability of the device through a charge supplement strategy. At the same time, the device size is reduced to the portable range, which is more suitable for the power needs of mobile or miniaturized sensor networks. The experimental results show that the output performance can be improved by decreasing the polar distance and increasing the rotational speed. At 600 rpm, the peak-to-peak output voltage, peak-to-peak output current and charge transfer of HPR-TENG are 3128 V, 221 μA and 492 nC, respectively. The output remains stable after 800,000 cycles, proving its excellent stability. The output power reaches a maximum of 344 mW at a load of 3 × 10^7 Ω HPR-TENG can collect kinetic and mechanical energy generated by a person to provide a stable power supply for cutting-edge high-voltage breakdown sensor systems, enabling simple and efficient inert gas or ultraviolet sensors. The proposed self-powered ultraviolet (UV) sensor, with its simple, low-cost design, has broad industrial and Internet of Things (IoT) applications, such as powering wearable health monitors, industrial condition sensors, and smart agriculture systems.

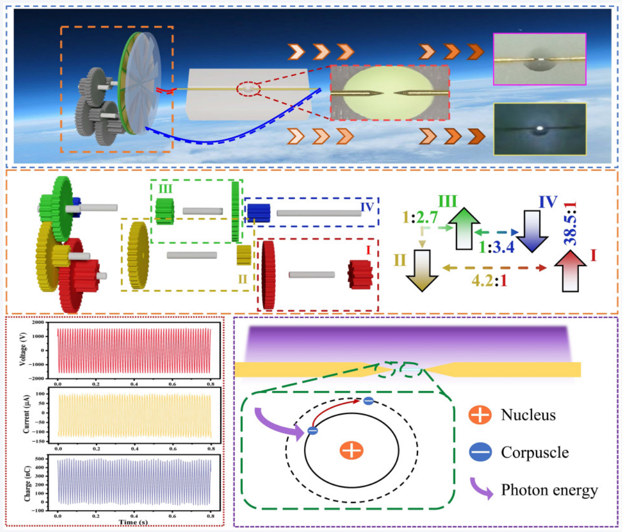

KEYWORDS: triboelectric nanogenerator, kinetic energy conversion, durability, ultraviolet sensor

1 Introduction

The Internet of Things (IoT) technology is developing rapidly and gradually penetrating into all aspects of our lives. With the further development of 5G, artificial intelligence, big data and other technologies, IoT will achieve greater breakthroughs and innovations in the future [1]. Many IoT devices and wireless sensor network systems [2–5] rely on battery power supply, but due to limited battery life, it is difficult to meet long-term operation needs even in low-power mode. IoT devices are often deployed in hard-to-reach places, making battery replacement, maintenance costs, and disposal of waste batteries a major challenge [6]. Therefore, sustainable energy harvesting technology has become an urgent requirement for the development of IoT [7].

In recent years, the triboelectric nanogenerator (TENG) [8] as a

Received: February 23, 2025; **Revised:** March 19, 2025
Accepted: March 24, 2025

✉Address correspondence to OliverChild@hotmail.com

new energy collection technique, because of its ability to convert mechanical energy efficient into electrical energy [9–13], has been widely concerned. Among them, the rotary triboelectric nanogenerator (R-TENG) has shown great potential in practical applications [14–22] due to its advantages of achieving high voltage and high-frequency output [23, 24]. Conventional R-TENG is prone to severe wear of the friction layer under high-frequency sliding friction, which limits its long-term stable operation [25]. Zhou et al. proposed an interfacial lubrication strategy between the friction layer and the electrode layer, which can reduce the friction loss and improve the output performance [26], but this method does not significantly improve the wear resistance. Lin et al. proposed a soft contact TENG, which is a non-contact TENG and significantly improves the wear resistance of the TENG [27]. However, the non-contact design leads to a decline in its output performance, which limits its application. Feng et al. proposed a simple charge refill strategy that greatly improves the output performance by adding a strip to the classic non-contact R-TENG structure, effectively solving the problem of low output performance of the non-contact TENG [28]. But the stability of the strip becomes low after long-term rotation, and the debris generated by the strip will pollute the friction layer, resulting in a sharp decline in power output performance. Hao et al. proposed a coaxial inversion TENG that uses wool instead of paper strips as the replenishment material, further improving the stability and output performance of the TENG [29]. However, the design of the coaxial reverse gear structure is large, need to be fixed on the platform, cannot be carried, need to be further improved. To achieve large-scale practical applications, the R-TENG needs to further improve output performance with increased wear resistance and simplify the structure to meet the practical needs of portable sensor devices.

In this study, we propose a high-performance press-driven rotation triboelectric nanogenerator (HPR-TENG), which uses a gear acceleration structure to achieve efficient energy conversion by pressing drive, and significantly improves the output performance and durability of the device through a charge supplement strategy. At the same time, by reducing the size of the device to the portable range, it is more suitable for the power needs of mobile or miniaturized sensor networks. The peak-to-peak output voltage of the HPR-TENG measured by oscilloscope is 3128 V [30, 31], the peak-to-peak output current is 221 μA, and the charge transfer is 492 nC (600 rpm). Moreover, the output remains stable after 800,000 cycles, with excellent stability and durability. Its output power reaches a maximum of 344 mW at a load of 3×10^7 Ω. The voltage output through the rectifier bridge takes only 0.68 s to charge a 100 μF capacitor to 5 V, and takes only 10 s to charge a 1000 μF capacitor to 5 V. The high-performance friction nanogenerator can also provide stable power supply for the cutting-edge high-voltage breakdown ultraviolet (UV) sensor system. Through the discharge phenomenon, it can be determined whether there is ultraviolet irradiation. In the future, through more in-depth research, it is expected to achieve a more accurate and convenient cutting-edge high-voltage breakdown sensor. The excellent output and portability of the HPR-TENG can be further improved in the future and installed in the sole or shoe of the robot to provide cushioning and mechanical energy harvesting to provide energy for wireless sensor network systems.

2 Results and discussion

2.1 Structural design and working principle

Figure 1(a) shows the overall system design of the HPR-TENG. The structure is accelerated by multi-stage gears, and the HPR-TENG is driven by the press of the human hand. After the acceleration of the mechanical structure, the rotor of the HPR-TENG can finally obtain a faster rotation speed and increase its output voltage, thus improving the efficiency of the breakdown of the tip of the needle. The complete model of the HPR-TENG is shown in Fig. S1 in the Electronic Supplementary Material (ESM). When pressure is applied to the pressing handle, the serrations at the end of the handle turn the internal gear accelerator. The specific mechanical structure model of the gear accelerator is shown in Fig. 1(b), which consists of three double-layer acceleration gears and one output gear. Gear I is driven by the press handle to drive gear II to rotate, gear II is in the sliding groove, when subjected to the force of gear I, gear II moves close to the direction of gear III, and engages with gear III to drive gear III to rotate, and finally gear III drives gear IV to rotate, each stage of gear is accelerated. Among them, the speed ratio of gear I and gear II is 1:4.2, the speed ratio of gear II and gear III is 1:2.7, the speed ratio of gear III and gear IV is 1:3.4, the speed ratio of these three stages of acceleration is 1:38.5; in addition, the speed ratio of the gear at the end of the handle and gear I is 1:3.9. A total of four stages of acceleration have been carried out, and the overall speed ratio is 1:150.15, which can make the HPR-TENG reach a faster speed at a slower pressing speed. The HPR-TENG stability test waveform after 500 s operation of the gear structure is shown in Fig. S3 in the ESM.

The structural decomposition diagram of HPR-TENG is shown in Fig. 1(c). The decomposition part is mainly divided into two parts, the rotor structure and the stator structure. The rotor structure is composed of an acrylic plate and eight polytetrafluoroethylene (PTFE) uniformly pasted on it, in which PTFE is a negative friction material. The stator part consists of a printed circuit board covered with 16 iso-spaced fan-shaped copper foils and a strip of wool pasted between the gaps of the copper foil, where the copper foil is a positive friction material and the wool is a positive charge supplement material. Eight copper foils separated from each other on the circuit board are connected together, divided into Cu1 and Cu2 groups. As a positive charge supplement material, wool not only increases the contact area with the negative friction material PTFE, increases the amount of charge on the surface of both, but also changes the direct contact friction between the rotor and the stator into soft contact friction, reducing the loss during operation. Figure 1(d) is the real photos of the rotor and stator of HPR-TENG.

The working principle of HPR-TENG is shown in Fig. 1(e). As the HPR-TENG rotates, it undergoes four distinct states. In state I, when $P_{(n+1)}$ is positioned above the electrodes of HPR-TENG$_{(n)}$ ($E_{HT(n)}$) and perfectly aligned with $E_{HT(n)}$, the negative friction material PTFE on the rotor has not yet contacted the wool on the stator. At this stage, only charge induction occurs with the Cu electrode, resulting in the maximum induced charge without any charge passing through the external circuit. As rotation continues and the $P_{(n+1)}$ part moves above $E_{HT(n+1)}$, the HPR-TENG enters state II. The negative friction material PTFE contacts the wool, causing ionization of amino acid residues in the wool's protein molecules. This ionization leads to an accumulation of positive

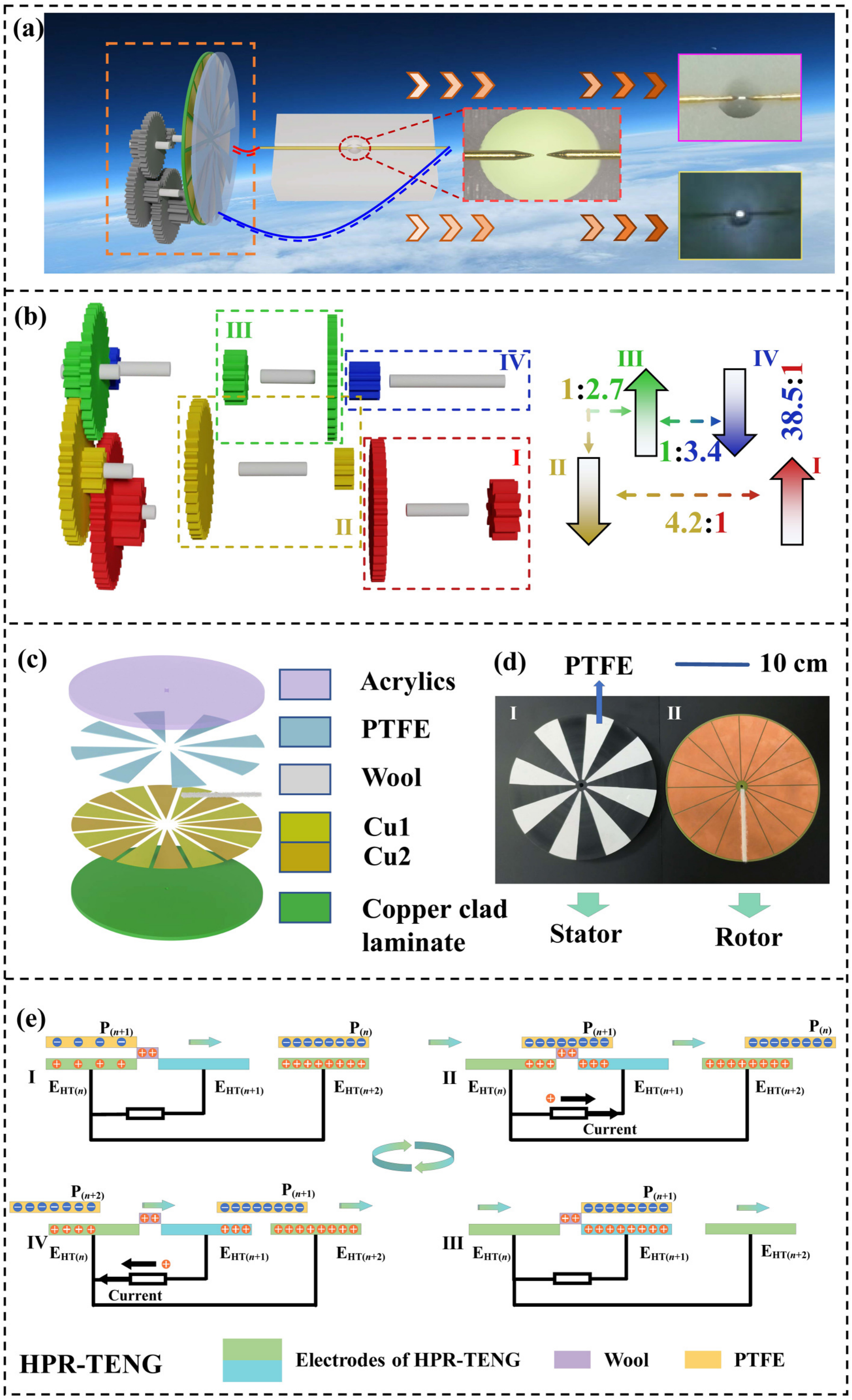

Figure 1 System scheme, structural design and working principle. (a) The overall system designs. (b) The mechanical structure physical model diagram of HPR-TENG. (c) HPR-TENG structure decomposition diagram. (d) A picture of the HPR-TENG stator and rotor. (e) Working principle of the HPR-TENG.

charges on the wool's surface and negative charges on the PTFE surface. The positive charge is transferred from $E_{HT(n)}$ to $E_{HT(n+1)}$. When $P_{(n+1)}$ fully aligns with $E_{HT(n+1)}$, the induced charge on $E_{HT(n+1)}$ peaks, and no charge flows through the external circuit. With the rotor advancing, the contact area between $E_{HT(n+1)}$ and $P_{(n+1)}$ gradually decreases, and the induced charge on $E_{HT(n+1)}$ gradually transfers to $E_{HT(n)}$. At the same time, the contact area between $P_{(n+1)}$ and $E_{HT(n+2)}$ increases, inducing charge between them transferring positive charges from $E_{HT(n+1)}$ to $E_{HT(n)}$, marking the transition to state IV. When $P_{(n+1)}$ aligns perfectly with $E_{HT(n+2)}$ as the rotor progresses, the HPR-TENG reverts to state I. Notably, the charge on the negative friction materials is retained effectively. Therefore, with each rotation cycle, the wool supplies the PTFE with additional charges, leading to a progressive increase in the HPR-TENG's electrical output. Assuming that the transfer of positive charge to $E_{HT(n+1)}$ is considered a positive current, the transfer to $E_{HT(n)}$ represents a negative current.

2.2 Performance characterization

In order to comprehensively study the effects of different variables on the electrical properties of HPR-TENG using PTFE and copper as electrodes, the electrical properties of HPR-TENG with different amounts of wool, different pole spacing and different rotation speeds were tested. The control variable method is used in the following experiments to ensure the reliability of the experimental data. When used as an independent variable, the wool is 1, the pole spacing is 1 mm, and the speed is 600 rpm. In the following experiment, when one of the parameters is selected as the independent variable, the remaining independent variables remain unchanged.

The output results of voltage and current selected by HPR-TENG with different wool quantity are shown in Figs 2(a) and 2(b), and the output results of charge transfer quantity are shown in Fig. S2(I) in the ESM. It can be seen from the figure that different amounts of wool have little influence on the output of HPR-TENG, which is almost negligible. Further analysis of the experimental data shows that the peak-peak output voltage of HPR-TENG with different wool quantity is 2999, 2999, 2914, 2999, and 2828 V respectively, while the peak-peak output current is 169.1, 155.8, 160.2, 166.3, and 152.2 μA, respectively. The experiment showed that the amount of wool had little effect on the output performance of HPR-TENG, so the subsequent experiment controlled the wool as one strip. Figure 2(c) shows the detailed output curves of voltage and current of HPR-TENG under the test condition of a wool as supplementary material.

Voltage and current output results of HPR-TENG under different pole spacing are shown in Figs. 2(d) and 2(e), and charge transfer output results are shown in Fig. S2(II) in the ESM. As can be seen from the figure, pole spacing has great influence on the performance of HPR-TENG. With the increasing of pole spacing from 1 to 4 mm, the voltage and current decrease sharply, and the decrease is the most when the pole spacing is from 1 to 2 mm. Further analysis of the experimental data shows that the output voltage peak-to-peak values of HPR-TENG with different pole spacing are 2913, 1799, 1370, and 856 V, respectively, and the output current peak-to-peak values are 229, 125, 96, and 74.2 μA, respectively. The experiment shows that the output performance of the HPR-TENG is inversely proportional to the pole spacing. The smaller the pole spacing, the better the output performance of HPR-TENG. In addition, too small pole spacing will accelerate the loss of the friction layer, resulting in a greatly shortened service life of the equipment. Therefore, it is important to find the pole spacing to ensure the long-term stable operation and high power output of the HPR-TENG. Figure 2(f) shows the detailed output curves of voltage and current of the HPR-TENG under the test condition of 1 mm pole spacing.

The output results of voltage, current and charge transfer at different speeds selected by HPR-TENG are shown in Figs. 3(a)–3(c). With the increase of speed, the output voltage and output current of HPR-TENG gradually increase. Further analysis of the experimental data shows that the peak-to-peak output voltage of HPR-TENG at different rotational speeds is 2314, 2528. 5, 2742, 2870, and 3128 V, respectively, and the peak-to-peak output current is 134, 161, 176, 195, and 221 μA. The maximum value of the output charge transfer is 484, 530, 522, 513, and 492 nC respectively. The experimental data show that the rotor speed is positively correlated with the output voltage and current of HPR-TENG, but has little effect on the charge transfer amount. This is because during the operation of HPR-TENG, the charge density generated by the storage electrode is related to its own material and does not change with the speed, so the amount of charge transfer does not change, but the increase of the speed leads to the increase of the frequency of charge transfer, so the output current increases with the increase of revolutions per minute. In order to obtain higher output performance, 600 rpm is selected as the general speed in the experiment with other variables. To more intuitively understand the output performance of the HPR-TENG, Fig. 3(d) shows the output voltage, current, and charge transfer curves of the

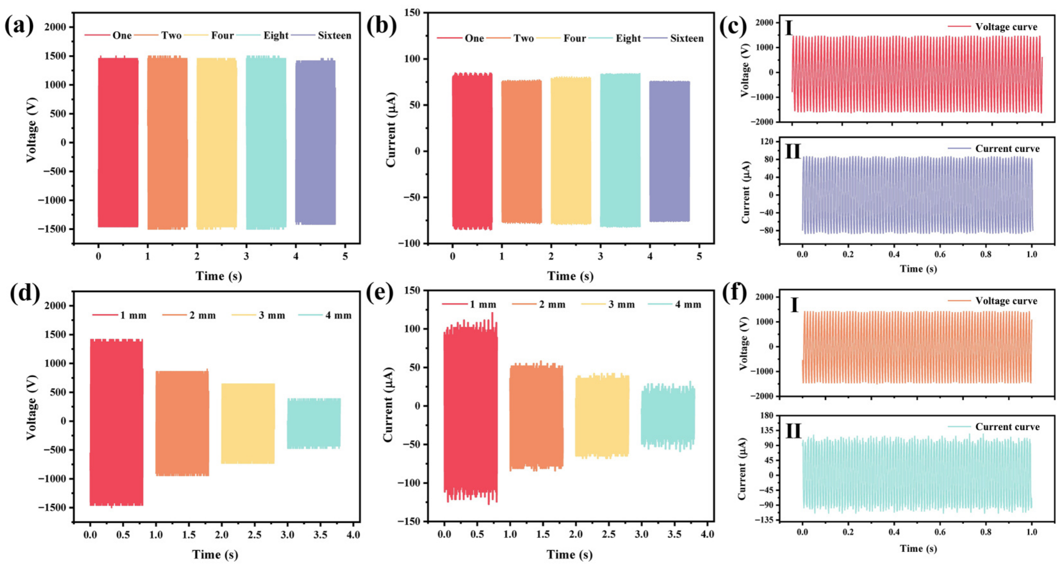

Figure 2 Performance characterization of wool with different number of strips and distance between electrodes. The output results of (a) voltage and (b) current of HPR-TENG under different wool quantity test conditions. (c) Detailed output curves of voltage and current for the HPR-TENG under test conditions with a wool as a supplementary material. The output results of (d) voltage and (e) current of the HPR-TENG under different test conditions with different pole spacing. (f) Detailed output curves of the voltage and current of the HPR-TENG under test conditions with pole spacing of 1 mm.

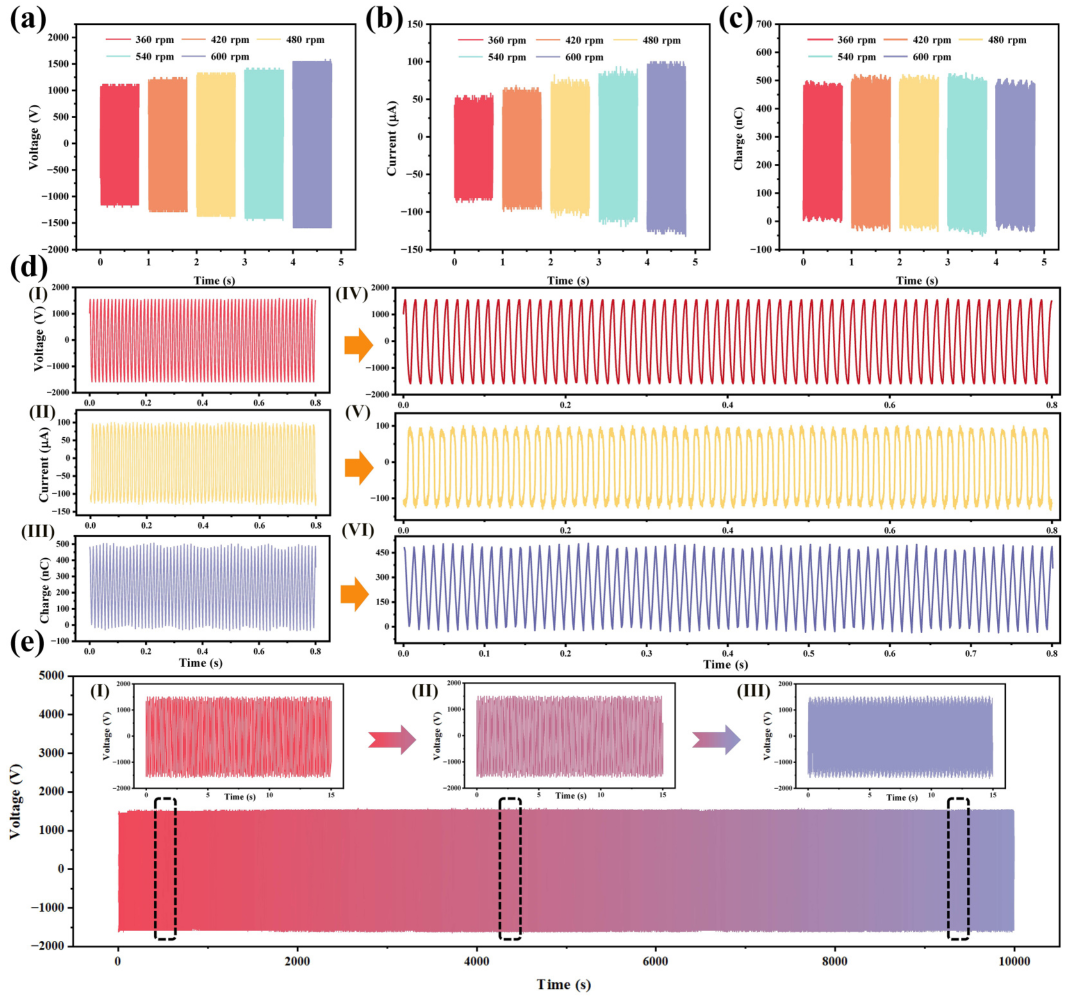

Figure 3 Performance characterization and stability test at different rotational speeds. The output results of (a) voltage, (b) current, and (c) charge transfer of HPR-TENG under different test conditions. (d) Output voltage, current and charge transfer curve of HPR-TENG at 600 rpm. (e) Stability test waveform for the HPR-TENG running for 10,000 s.

HPR-TENG at 600 rpm. Figures 3(d)(I)–3(d)(III) show thumbnail images of output voltage, current and charge transfer respectively, while Figs. 3(d)(IV)–3(d)(VI) show detailed images of output voltage, current and charge transfer respectively.

In order to test the stability of the HPR-TENG, the equipment was run for 10,000 s under the test conditions of one wool, pole spacing of 1mm and 600 rpm. The test results are shown in Fig. 3(d). The output performance of HPR-TENG remains stable and the output curve fluctuates very little during the longtime test. In Fig. 3(d), Figs. 3(d)(I)–3(d)(III) show the detailed output voltage of the HPR-TENG when it is working for about 50, 5000, and 9050 s, respectively, which further demonstrates the strong stability of the HPR-TENG. In summary, through the wool charging strategy, the HPR-TENG can achieve efficient output performance at small pole spacing and high rotational speed, and achieve superior stability in the soft contact operating mode, showing its great potential in practical applications.

2.3 Application

In order to study the influence of different load sizes on the output performance of HPR-TENG, load experiments were carried out with resistors ranging from 1 to 1×10^{12} Ω. The experimental conditions were set as 1 wool with pole spacing of 1 mm and rotating speed of 600 rpm. The fitting curve of HPR-TENG output voltage and current amplitude changes under different loads is shown in Fig. 4(a). When the load resistance is within the range of 10^6–10^8 Ω, the voltage and current at both ends of the load end change most obviously, and the voltage decreases rapidly with the rapid increase of current. The output power of the HPR-TENG is calculated as described in Note S1 in the ESM. The corresponding power under different load resistors is obtained by the above power calculation method. The power output variation curve of HPR-TENG under different load conditions is shown in Fig. 4(b). When the load is 3×10^7 Ω, the output power reaches the maximum value of 344 mW. The area of copper stator used in the experiment is 0.0314 m^2, and the calculated power density is 10.1 W/m^2. Comparison of the output power for different TENGs is shown in Table S1 in the ESM.

In order to verify the electrical performance of HPR-TENG, the charging performance of HPR-TENG was tested. Since the signal generated by the HPR-TENG is an alternating current (AC) signal, it needs to be converted to a direct current (DC) signal for easy testing. In this experiment, a bridge rectifier circuit is used to rectify the output signal in order to charge the capacitor. A fully charged capacitor is connected to the load by a single-pole double-throw switch to provide power. Figure 4(c) shows the charging strategy

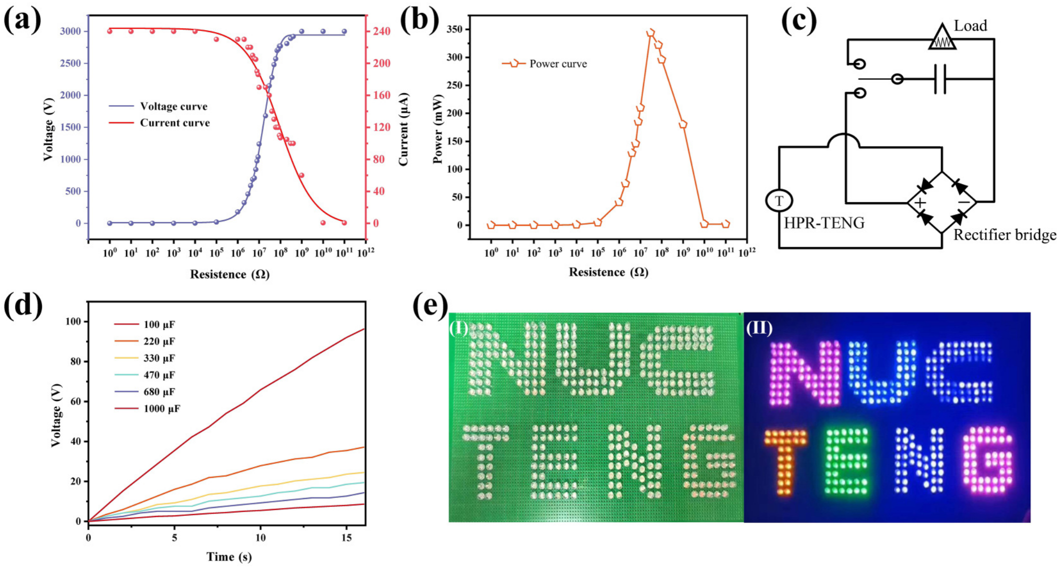

Figure 4 Application. (a) The volt–current variation curves of HPR-TENG with recharge strategy under different load conditions. (b) Power output variation curves of HPR-TENG with recharge strategy under different load conditions. (c) Charging strategy and power management circuit diagram of HPR-TENG. (d) Charging characteristics of the HPR-TENG under different capacitors after passing the power management circuit. (e) HPR-TENG lights an image composed of LED lights.

and power management circuit diagram of the HPR-TENG [32–37]. During the experiment, the capacitors of 100, 220, 330, 470, 680, and 1000 μF were charged, and their charging characteristics were shown in Fig. 4(d). Further analysis of the experimental data shows that after 15 s of charging, the voltage of the above capacitors reaches 92, 35.5, 23.6, 18.6, 12.7, and 8 V respectively. Among them, it takes only 0.68 s to charge a 100 μF capacitor to 5 V, and 10 s to charge a 1000 μF capacitor to 5 V. In order to further test the output performance of the HPR-TENG, it is used to drive a light array composed of light-emitting device (LED) lights. Figures 4(e)(I) and 4(e)(II) show the lighting of LED arrays in light and dark environments respectively.

In order to study the effect of ultraviolet irradiation on the needle tip discharge driven by HPR-TENG [38, 39], an experimental platform was built as shown in Fig. S3 in the ESM, and the schematic diagram of ultraviolet irradiation on needle tip is shown in Fig. 5(a). The size of the tip used in the experiment is shown in Fig. S4 in the ESM. The material is gold-plated copper, which can enhance the oxidation resistance of the needle tip. Fix the tip of the needle on the insulated resin base and set its spacing to 200 μm under the microscope. Select a UV lamp with a wavelength of 254 nm to illuminate the needle tip. Figure 5(b) shows the schematic diagram of the needle tip ultraviolet sensor. Ultraviolet light mainly affects gold atoms and particles in the air, and ultimately affects the performance of the needle tip discharge. For gold atoms, ultraviolet light can excite the core electrons of gold to enter a higher energy level or leave the atom. Also for particles in the air, oxygen atoms have the smallest ionization energy, and ultraviolet energy can excite electrons in oxygen and other gas

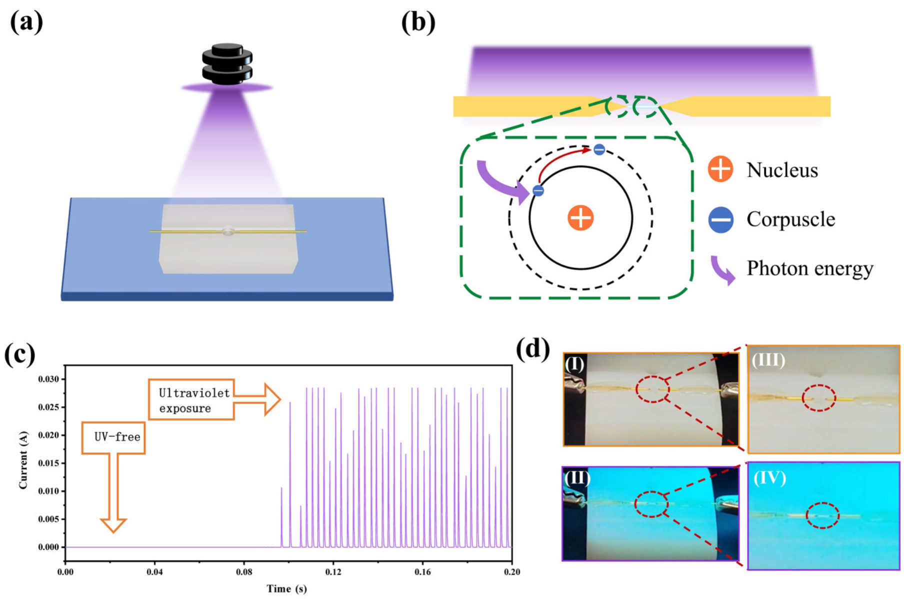

Figure 5 HPR-TENG-driven pinhead UV sensor. (a) Diagram of UV irradiation of needle tip. (b) Working principle diagram of needle tip UV sensor. (c) Current curve of discharge before and after ultraviolet irradiation. (d) The physical comparison picture of the needle tip sensor before and after ultraviolet irradiation.

components to a higher energy level, thereby reducing the breakdown threshold of the needle tip and increasing the possibility of breakdown. The current curve generated by discharge before and after ultraviolet irradiation is shown in Fig. 5(c). Before ultraviolet irradiation, the energy provided by the HPR-TENG is not enough to puncture the tip, and there is no output current. After ultraviolet irradiation, the difficulty of needle breakdown is reduced, resulting in high-frequency needle breakdown. Figure 5(d) is the physical comparison picture of the needle tip before and after ultraviolet irradiation. Specifically, Figs. 5(d)(I) and 5(d)(III) show a scenario in which no tip breakdown occurs without ultraviolet light, and Figs. 5(d)(II) and 5(d)(IV) show a scenario in which tip breakdown occurs under ultraviolet light. The results show that UV irradiation significantly reduces the breakdown threshold of the tip driven by HPR-TENG, and promotes the high frequency discharge of the tip. This finding has important implications for optimizing tip discharge performance and the design of related electrical devices such as ultraviolet sensors.

3 Conclusion

In this study, a high-performance press-driven triboelectric nanogenerator was designed and developed. The design adopts a gear acceleration structure, which can realize automatic meshing and separation, so that the HPR-TENG can achieve smooth and efficient output, at the same time, the traditional TENG can be shrunk to a portable size, greatly improving its portability. Through a soft contact friction strategy, the HPR-TENG uses a combination of PTFE and wool to reduce direct contact friction, reduce energy loss and extend the service life of the equipment. The wool recharge strategy effectively replenishes the charge and improves the charge exchange efficiency, thus achieving higher output power and long-term stable operation at the same speed. In this experiment, the optimal output performance was achieved under the condition of 1 wool, pole spacing of 1mm and rotating speed of 600 rpm. The output signals reached 3128 V, 221 μA and 492 nC respectively. At the same time, due to the soft contact friction between the electrodes, the durability is very good, and the output performance remains stable after 10,000 s, or 800,000 cycles. In addition, in the impedance matching experiment, the output power reaches a maximum of 344 mW at a load of 3×10^7 Ω, and the output power density is 10.1 W/m^2. The voltage output through the rectifier bridge takes only 0.68 s to charge a 100 μF capacitor to 5 V, and takes only 10 s to charge a 1000 μF capacitor to 5 V. It can also easily light the LED array to supply energy for its work. The high-performance triboelectric nanogenerator can also provide stable power supply for the cutting-edge high-voltage breakdown UV sensor system. Through the discharge phenomenon, it can be determined whether there is ultraviolet irradiation. After further study, it is expected to achieve a more accurate and more convenient ultraviolet sensor. In the future, the HPR-TENG can also be truly added to the sole and exoskeleton, giving full play to its advantages of portability, high pressure and self-powered.

4 Experimental section

4.1 Accelerate the design and manufacture of mechanical structures

The acceleration mechanical structure has four stages of acceleration, which is composed of a handle the gear at the end of the handle, three double-layer gears, and an output gear. The parameters of the the gear at the end of the handle in S1 are: modulus 0.8, number of teeth 39 (9 teeth reserved), and end width 2.3 mm. In Fig. 1(b), the upper gear parameters of gear I are: modulus 0.8, number of teeth 10, and end width 4 mm. The lower gear parameters are: modulus 0.5, number of teeth 42, end width 2 mm. The upper and lower gear modules of gears II, III and IV are 0.5, the number of teeth are respectively upper II: 10, lower II: 38, upper III: 14, lower III: 34, IV: 10, and the end width is respectively upper II: 2.85 mm, lower II: 1.75 mm, upper III: 3.1 mm, lower III: 1.4 mm, IV: 4.85 mm. The shaft diameter of each of the four gears is 2 mm. The press handle is made of three-dimensional (3D)-printed aluminum alloy and the gear is commercially purchased.

4.2 Design and manufacture of high performance triboelectric nanogenerator

The rotor is a laser-cut acrylic plate with a radius of 10 cm, the stator is a printed circuit board covered with 16 iso-spaced fan-shaped copper foils, and the negative friction material and charge supplement material wool are commercially purchased.

4.3 Characterizations and measurements

The short-circuit current, amount of charge transfer and internal resistance of HPR-TENG were measured with an electrostatic meter (Keithley 6514 with an equivalent impedance of 10 kΩ), and the open-circuit voltage was measured with an oscilloscope (DS7054 500Mhz 10GSa/s RIGOL) and a high-voltage probe (P5100A with an equivalent impedance of 40 MΩ Tektronix) were measured.

Electronic Supplementary Material: Supplementary material (HPR-TENG structure diagram, charge transfer amounts of different spacing and different wool bar numbers, stability test data, needle tip data, experimental platform, calculation formulas, and performance comparison) is available in the online version of this article at https://doi.org/10.26599/NR.2025.94907401.

Data availability

All data needed to support the conclusions in the paper are presented in the manuscript and the Electronic Supplementary Material. Additional data related to this paper may be requested from the corresponding author upon request.

Acknowledgements

We gratefully acknowledge support from the National Natural Science Foundation of China (No. 62405294).

Declaration of competing interest

All the contributing authors report no conflict of interests in this work

Author contribution statement

T. M. R.: Data curation, validation, writing manuscript, models and principle design, writing manuscript. Z. K.W., C. C. H., and M. Z. C.: Validation and writing manuscript. C. Z., Y. Q. Z., and C. Y. X.: Data curation, validation, project administration, funding acquisition. All the authors have approved the final manuscript.

Use of AI Statement

None.

References

[1] Xu, L. D.; He, W.; Li, S. C. Internet of Things in industries: A survey. *IEEE Trans. Ind. Inf.* **2014**, *10*, 2233–2243.

[2] Akhtar, F.; Rehmani, M. H. Energy replenishment using renewable and traditional energy resources for sustainable wireless sensor networks: A review. *Renewable Sustainable Energy Rev.* **2015**, *45*, 769–784.

[3] Priyadarshi, R. Energy-efficient routing in wireless sensor networks: A meta-heuristic and artificial intelligence-based approach: A comprehensive review. *Arch. Comput. Methods Eng.* **2024**, *31*, 2109–2137.

[4] Rault, T.; Bouabdallah, A.; Challal, Y. Energy efficiency in wireless sensor networks: A top-down survey. *Comput. Netw.* **2014**, *67*, 104–122.

[5] Ryu, H.; Yoon, H. J.; Kim, S. W. Hybrid energy harvesters: Toward sustainable energy harvesting. *Adv. Mater.* **2019**, *31*, 1802898.

[6] Hao, C. C.; Qi, B. W.; Wang, Z. K.; Cai, M. Z.; Cui, J.; Zheng, Y. Q. High performance rotating triboelectric nanogenerator with coaxial rolling charge pump strategy. *Micromachines* **2023**, *14*, 2160.

[7] Shaikh, F. K.; Zeadally, S. Energy harvesting in wireless sensor networks: A comprehensive review. *Renewable Sustainable Energy Rev.* **2016**, *55*, 1041–1054.

[8] Wang, Z. L. Triboelectric nanogenerators as new energy technology and self-powered sensors—Principles, problems and perspectives. *Faraday Discuss.* **2014**, *176*, 447–458.

[9] Wang, W. L.; Yang, D. F.; Yan, X. R.; Wang, L. C.; Hu, H.; Wang, K. Triboelectric nanogenerators: The beginning of blue dream. *Front. Chem. Sci. Eng.* **2023**, *17*, 635–678.

[10] Zhang, C. G.; Hao, Y. J.; Yang, J. Y.; Su, W.; Zhang, H. K.; Wang, J.; Wang, Z. L.; Li, X. H. Recent advances in triboelectric nanogenerators for marine exploitation. *Adv. Energy Mater.* **2023**, *13*, 2300387.

[11] Liu, Z.; Li, H.; Shi, B. J.; Fan, Y. B.; Wang, Z. L.; Li, Z. Wearable and implantable triboelectric nanogenerators. *Adv. Funct. Mater.* **2019**, *29*, 1808820.

[12] Pu, X.; Zhang, C.; Wang, Z. L. Triboelectric nanogenerators as wearable power sources and self-powered sensors. *Natl. Sci. Rev.* **2023**, *10*, nwac170.

[13] Zhou, L. L.; Liu, D.; Wang, J.; Wang, Z. L. Triboelectric nanogenerators: Fundamental physics and potential applications. *Friction* **2020**, *8*, 481–506.

[14] Du, T. L.; Dong, F. Y.; Xi, Z. Y.; Zhu, M. X.; Zou, Y. J.; Sun, P. T.; Xu, M. Y. Recent advances in mechanical vibration energy harvesters based on triboelectric nanogenerators. *Small* **2023**, *19*, 2300401.

[15] Huang, Y.; Du, T. L.; Xiang, C.; Zhang, Y.; Si, J. C.; Yu, H. Y.; Yuan, H. C.; Sun, P. T.; Xu, M. Y. Research progress of acoustic energy harvesters based on nanogenerators. *Int. J. Energy Res.* **2023**, *2023*, 5568046.

[16] Hurdoganoglu, D.; Safaei, B.; Cheng, J.; Qin, Z. Y.; Sahmani, S. A comprehensive review on the novel principles, development and applications of triboelectric nanogenerators. *Appl. Mech. Rev.* **2024**, *76*, 010802.

[17] Lu, S.; Gao, L. X.; Chen, X.; Tong, D. Q.; Lei, W. Q.; Yuan, P. F.; Mu, X. J.; Yu, H. Simultaneous energy harvesting and signal sensing from a single triboelectric nanogenerator for intelligent self-powered wireless sensing systems. *Nano Energy* **2020**, *75*, 104813.

[18] Tian, J. W.; Chen, X. Y.; Wang, Z. L. Environmental energy harvesting based on triboelectric nanogenerators. *Nanotechnology* **2020**, *31*, 242001.

[19] Wang, Z. K.; Cui, J.; Liu, T. S.; Bai, S. M.; Hao, C. C.; Zheng, Y. Q.; Xue, C. Y. Composited pressure-velocity sensor based on sandwich-like triboelectric nanogenerator for smart traffic monitoring. *IEEE Sens. J.* **2023**, *23*, 27872–27884.

[20] Zhu, M. L.; Yi, Z. R.; Yang, B.; Lee, C. Making use of nanoenergy from human-nanogenerator and self-powered sensor enabled sustainable wireless IoT sensory systems. *Nano Today* **2021**, *36*, 101016.

[21] Yang, Y. Q.; Guo, X. G.; Zhu, M. L.; Sun, Z. D.; Zhang, Z. X.; He, T. Y. Y.; Lee, C. Triboelectric nanogenerator enabled wearable sensors and electronics for sustainable internet of things integrated green earth. *Adv. Energy Mater.* **2023**, *13*, 2203040.

[22] Wen, H. Y.; Yang, X. Y.; Huang, R. Y.; Zheng, D.; Yuan, J. B.; Hong, H. X.; Duan, J. L.; Zi, Y. L.; Tang, Q. W. Universal energy solution for triboelectric sensors toward the 5G era and internet of things. *Adv. Sci.* **2023**, *10*, 2302009.

[23] Lin, L.; Wang, S. H.; Xie, Y. N.; Jing, Q. S.; Niu, S. M.; Hu, Y. F.; Wang, Z. L. Segmentally structured disk triboelectric nanogenerator for harvesting rotational mechanical energy. *Nano Lett.* **2013**, *13*, 2916–2923.

[24] Jiang, T.; Chen, X. Y.; Yang, K. D.; Han, C. B.; Tang, W.; Wang, Z. L. Theoretical study on rotary-sliding disk triboelectric nanogenerators in contact and non-contact modes. *Nano Res.* **2016**, *9*, 1057–1070.

[25] Cai, M. Z.; Hao, C. C.; Wang, Z. K.; Zhai, C.; Zheng, Y. Q.; Xue, C. Y. High performance rotary triboelectric nanogenerator based on wool charge supplementation strategy with low wear. *Sci. China Technol. Sci.* **2024**, *67*, 3535–3545.

[26] Zhou, L. L.; Liu, D.; Zhao, Z. H.; Li, S. X.; Liu, Y. B.; Liu, L.; Gao, Y. K.; Wang, Z. L.; Wang, J. Simultaneously enhancing power density and durability of sliding-mode triboelectric nanogenerator via interface liquid lubrication. *Adv. Energy Mater.* **2020**, *10*, 2002920.

[27] Lin, Z. M.; Zhang, B. B.; Zou, H. Y.; Wu, Z. Y.; Guo, H. Y.; Zhang, Y.; Yang, J.; Wang, Z. L. Rationally designed rotation triboelectric nanogenerators with much extended lifetime and durability. *Nano Energy* **2020**, *68*, 104378.

[28] Feng, H. Q.; Bai, Y.; Qiao, L.; Li, Z.; Wang, E. G.; Chao, S. Y.; Qu, X. C.; Cao, Y.; Liu, Z.; Han, X. et al. An ultra-simple charge supplementary strategy for high performance rotary triboelectric nanogenerators. *Small* **2021**, *17*, e2101430.

[29] Hao, C. C.; Wang, Z. K.; Cai, M. Z.; Liu, T. S.; Zhai, C.; Cui, J.; Zheng, Y. Q.; Xue, C. Y. High-performance coaxial reversal rotational triboelectric nanogenerator based on charge pumping strategy driving tip high voltage breakdown. *Nano Energy* **2024**, *128*, 109857.

[30] Zhang, W. H.; Gu, G. Q.; Qin, H. F.; Li, S. M.; Shang, W. Y.; Wang, T. Y.; Zhang, B.; Cui, P.; Guo, J. W.; Yang, F. et al. Measuring the actual voltage of a triboelectric nanogenerator using the non-grounded method. *Nano Energy* **2020**, *77*, 105108.

[31] Zhang, W. H.; Gu, G. Q.; Shang, W. Y.; Luo, H. C.; Wang, T. Y.; Zhang, B.; Cui, P.; Guo, J. M.; Yang, F.; Cheng, G. et al. A general charge compensation strategy for calibrating the voltage of a triboelectric nanogenerator measured by a capacitive circuit. *Nano Energy* **2021**, *86*, 106056.

[32] Gu, G. X.; Gu, G. Q.; Shang, W. Y.; Zhang, Z. H.; Zhang, W. H.; Wang, C.; Fang, D. Y.; Cheng, G.; Du, Z. L. The self-powered agricultural sensing system with 1.7 km wireless multichannel signal transmission using a pulsed triboelectric nanogenerator of corn husk

composite film. *Nano Energy* **2022**, *102*, 107699.
[33] Qin, H. F.; Gu, G. Q.; Shang, W. Y.; Luo, H. C.; Zhang, W. H.; Cui, P.; Zhang, B.; Guo, J. M.; Cheng, G.; Du, Z. L. A universal and passive power management circuit with high efficiency for pulsed triboelectric nanogenerator. *Nano Energy* **2020**, *68*, 104372.
[34] Shang, W. Y.; Gu, G. Q.; Zhang, W. H.; Luo, H. C.; Wang, T. Y.; Zhang, B.; Guo, J. M.; Cui, P.; Yang, F.; Cheng, G. et al. Rotational pulsed triboelectric nanogenerators integrated with synchronously triggered mechanical switches for high efficiency self-powered systems. *Nano Energy* **2021**, *82*, 105725.
[35] Wang, T. Y.; Wang, C.; Zeng, Q. X.; Gu, G. Q.; Wang, X.; Cheng, G.; Du, Z. L. A real-time, self-powered wireless pressure sensing system with efficient coupling energy harvester, sensing, and communication modules. *Nano Energy* **2024**, *125*, 109533.
[36] Zhang, W. H.; Gu, G. Q.; Zhang, Z. H.; Ren, H. X.; Zhou, H. Y.; Gui, Y. Y.; Du, Z. L.; Cheng, G. Enhancing the output energy of triboelectric nanogenerator by adaptive arc discharge devices and its application in wireless weather sensing system. *Nano Energy* **2024**, *129*, 109987.
[37] Zhang, Z. H.; Gu, G. Q.; Zhang, W. H.; Gu, G. X.; Shang, W. Y.; Liu, Y.; Cheng, G.; Du, Z. L. Double loops power management circuit of pulsed triboelectric nanogenerator with enhanced efficiency at low operating voltage and its application in self-powered flue gas monitoring system. *Nano Energy* **2023**, *110*, 108360.
[38] Liu, T. S.; Cui, J.; Zheng, Y. Q.; Bai, S. M.; Hao, C. C.; Xue, C. Y. A self-powered inert-gas sensor based on gas ionization driven by a triboelectric nanogenerator. *Nano Energy* **2023**, *106*, 108083.
[39] Zhai, C.; Chou, X. J.; He, J.; Song, L. L.; Zhang, Z. X.; Wen, T.; Tian, Z. M.; Chen, X.; Zhang, W. D.; Niu, Z. C. et al. An electrostatic discharge based needle-to-needle booster for dramatic performance enhancement of triboelectric nanogenerators. *Appl. Energy* **2018**, *231*, 1346–1353.